Probabilistic approach to assess URM walls with openings using discrete rigid block analysis (D-RBA)

Bora Pulatsu [a,*], Semih Gonen [b], Fulvio Parisi [c], Ece Erdogmus [d], Kagan Tuncay [e], Marco Francesco Funari [f], Paulo B. Lourenço [g]

[a] *Department of Civil and Environmental Engineering, Carleton University, Canada*
[b] *Department of Civil Engineering and Energy Technology, Oslo Metropolitan University, Norway*
[c] *Department of Structures for Engineering and Architecture, University of Naples Federico II, Italy*
[d] *School of Building Construction, Georgia Institute of Technology, United States*
[e] *Civil Engineering, Middle East Technical University, Turkey*
[f] *Civil and Environmental Engineering, University of Surrey, United Kingdom*
[g] *Civil Engineering, University of Minho, Portugal*

A B S T R A C T

This study aims to improve our current understanding of the seismic assessment of load-bearing unreinforced masonry (URM) systems by proposing a probabilistic computational modeling framework using the discrete element method (DEM). The main objective is to predict the structural behavior and capacity of URM walls with openings subjected to lateral loading, considering uncertainties in material properties. The proposed modeling strategy represents masonry as an assembly of rigid blocks interacting along their boundaries by adopting the point-contact hypothesis. Fracture energy-based softening contact models are implemented into a commercial discrete element code (3DEC) to better simulate both the pre- and post-peak behavior of masonry. The results highlight the influence of material properties on the force capacity, displacement capacity (drift limits), and collapse mechanisms of walls with openings. Based on the applied non-spatial probabilistic analyses, the most commonly observed failure mechanisms are further assessed using a simplified macro-block formulation. As a result, practical, yet necessary, inferences are made, providing valuable contributions. Furthermore, the validated discontinuum analysis framework is demonstrated as an accurate structural analysis strategy and a useful approach to simulating the potential collapse mechanism of load-bearing URM structures.

1. Introduction

Unreinforced masonry (URM) buildings constitute the majority of cultural heritage and residential buildings worldwide, especially in high seismicity zones [1]. The characteristics and structural behavior of these structures vary remarkably based on the type of building material (*e.g.*, stone, brick, adobe, etc.) and construction technique (workmanship). Although existing URM buildings provide many favorable features (*e.g.*, durability, fire safety, high thermal mass for energy conservation, etc.), they are vulnerable to seismic actions due to their high mass, the weak tensile strength of masonry compared to its compression strength, and, often, low-quality construction practices. In this regard, recent and past earthquakes indicated the poor seismic performance of existing URM

buildings due to the low construction quality and improper connections between structural components [2–4].

Post-seismic event surveys reveal that URM buildings suffer from various damage patterns related to in-plane and out-of-plane directions [5]. When out-of-plane failures are prevented, in-plane damage may develop under lateral forces governed by the in-plane lateral capacity of walls and pier-spandrel systems. The seismic capacity of masonry walls relies on their material properties, boundary conditions, vertical (compression) loads, slenderness ratios, and wall cross-section morphologies, as discussed in the literature [6–11]. In parallel with URM walls, pier-spandrel systems representing walls with openings are sensitive to these factors but require special attention to assess the coupling effect between the spandrels and piers, where spandrels work as a horizontal element transferring forces between the piers.

In contrast to the vast amount of studies on masonry walls, knowledge of masonry spandrels is limited [12]. Recent research focuses on the strength estimation [13], or experimental and numerical behavior of masonry spandrels [14–16], which significantly contributed to the understanding of mechanics and in-plane capacity. The coupling effect between piers and spandrels was also investigated [17], and the behavior of pier-spandrel systems was further studied via laboratory tests and detailed micro-models [18–21]. Moreover, the influence of the spandrel configuration was examined for various lintel types [22,23]. However, most of the mentioned numerical studies do not consider the uncertainty in material properties and their impact on the structural behavior and capacity of pier-spandrel systems. This research gap. which is the main motivation of the current study, necessitates a more accurate and efficient modeling strategy, further explained in the next section.

2. URM pier-spandrel systems and research motivation

Masonry is a composite, orthotropic and non-linear material consisting of units and mortar. From the computational modeling perspective, each feature adds to the complexity of structural modeling of masonry buildings, proving accurate capacity predictions challenging. Typically, global collapse mechanisms of masonry structures result from successive developments of local failures at the mortar joints, referred to as weak joints, due to considerable differences in stiffness and strength parameters of masonry constituents. This phenomenon is explicitly considered in the proposed modeling strategy to capture crack localization induced by lateral seismic forces, based on the discrete element method (DEM). The schematization of the workflow is represented in Fig. 1.

Recent advances in DEM-based modeling of masonry structures provide different computational frameworks, as recently presented by the authors of this paper and other researchers with different levels of complexity and accuracy [8,24–26]. It is also worth noting that the application of discrete element modeling has a wide spectrum, from macro-scale collapse analysis of masonry infrastructures to micro-scale fracture simulations of quasi-brittle construction materials [11,27–33]. The common feature among all discrete element models is that the material (or the structural element) is considered as a distinct body or system of bodies, which may be rigid or deformable. Hence, the computational cost is proportional to the number of distinct bodies utilized in the simulation and whether they are rigid or deformable.

This study utilizes a discontinuum-based modeling approach to simulate an unreinforced masonry pier-spandrel system based on the simplified micro-modeling representation of brickwork assemblage aligned with the previous studies [34–36]. The complex structural behavior of URM pier-spandrel systems is investigated using a validated computational model. Additionally, the inherent uncertainty of material properties is considered to estimate its influence on the global behavior and collapse mechanism. This research compromises the computational cost and accuracy by presenting an alternative approach, utilizing rigid blocks with fracture-energy-based contact constitutive models referred to as discrete rigid block analysis (D-RBA). To simulate all potential failure mechanisms, together with their probability of occurrence, the authors present a probabilistic framework integrated with D-RBA and discuss each collapse mode with associated drift limits. Therefore, the proposed modeling approach and results contribute to the seismic analysis of URM buildings that can be utilized to prevent partial failures, life-threatening collapses, and future loss of cultural heritage. Further, more accurate computational models will lead to better future interventions for maintaining or strengthening existing masonry structures as well as masonry debris distribution/impact analysis beyond near collapse (*e.g.* Ref. [37]).

The organization of the manuscript is as follows: in Sect. 2, the mathematical background and computational procedure of D-RBA are presented. The performed validation study is explained in Sect. 3, where the advantageous features of the proposed modeling
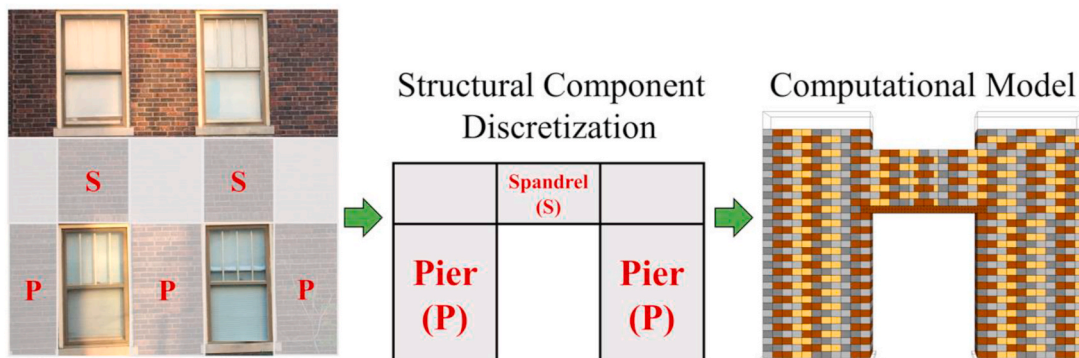

Fig. 1. Pier-spandrel system and corresponding DEM-based computational model.

approach and modeling details are highlighted and discussed. In Sect. 4, the data selection procedure is explained, and the stochastic analyses are carried out. The obtained distinct failure modes are discussed, and the effects of variable material properties on the behavior are investigated. According to the probabilistic D-RBA results, in Sect. 5, drift limits for different failure mechanisms are discussed and compared with the previous numerical solutions and experiments. Additionally, in Sect. 6, a simplified macro-block approach is proposed based on kinematic limit analysis to assess the same wall with an opening, and the results are compared against the obtained probabilistic solutions. Finally, Sect. 7, provides the highlights of this study, while conclusions, and potential areas for future works are given in Sect. 8.

3. Discrete rigid block analysis (D-RBA): computational framework

Computational modeling of masonry structures can be categorized under two groups, i.e., continuum and discontinuum-based solutions. While the former approach typically represents the composite structure of masonry as a homogeneous isotropic material, the latter explicitly considers the weak joints in the numerical formulation. Different discontinuum types of analysis have been proposed in the literature within the last several decades, namely the non-smooth contact dynamics method (NSCD), the discontinuous deformation analysis (DDA), and the combined finite-discrete element method (FDEM) [38–41]. This study uses another discontinuum-based approach using the discrete element method (DEM), first presented by Cundall [42]. The core idea of DEM relies on the integration of equations of motion for rigid or deformable bodies (replicating a discontinuous media) that can mechanically interact with each other based on contact stress-displacement laws. A dynamic solution algorithm is followed during analysis, in which the integrated motion equations provide new velocities and block positions that are utilized to calculate new contact forces. Then, the obtained contact forces are applied to the blocks in the next step, and equations of motion are solved for new velocities again [43]. The explained mechanical calculation cycle continues until the quasi-static solution (if any) is reached.

The choice of rigid or deformable blocks in DEM-based models directly depends on the physics of the problem, deemed simplifications, and the available computational power. Here, rigid blocks are utilized to replicate the masonry units, whereas mortar joints are represented as zero-thickness interfaces, as shown in Fig. 2. The dimensions of the rigid blocks in the discrete element model are expanded up to the half-thickness of the mortar joints, classified as a simplified micro-model [34]. Note that a masonry unit consists of two equal rigid blocks in contact, sharing the same potential cracking surface (see Fig. 2).

The proposed D-RBA assumes that the deformation can only occur at the joints between the blocks. Each rigid block has 6° of freedom (3 translations and 3 rotational). The integration of translational and rotational equations of motion is performed via the explicit central difference method and solved for each rigid block centroid in the system. The new translational ($\dot{u}_i^{t+}$) and rotational (ω^{t+}) velocities (evaluated at the mid-intervals of a time step, Δt; $t^+ = t + \Delta t/2$, $t^- = t - \Delta t/2$) are computed as follows:

$$\dot{u}_i^{t+} = \dot{u}_i^{t-} + \frac{\Delta t}{m}\left(\Sigma F_i^t - \lambda |F_i^t| sgn(\dot{u}^{t-})\right) \tag{1}$$

$$\omega_i^{t+} = \omega_i^{t-} + \frac{\Delta t}{I}\left(\Sigma M_i^t - \lambda |M_i^t| sgn(\omega^{t-})\right) \tag{2}$$

where F, M, I, and λ are the force vector, including the sum of contact forces and applied forces (*e.g.*, self-weight), moment vector, consisting of moments developed by contact forces and applied forces, mass moments of inertia and non-dimensional damping constant (default value is 0.8), respectively. Moreover, m and g stand for block mass and gravitational acceleration vectors. For quasi-static analysis, the viscous damping parameter is adjusted to obtain steady-state solutions (either corresponding to equilibrium or steady-state failure (collapse)) using the local-damping formulation discussed in the reference study [44]. Note that the adopted damping algorithm is proportional to the unbalanced force (ΣF) and moment (ΣM) opposing to the motion depending on the velocity vector ($sgn(\xi) = 1$, if $\xi \geq 0$, $sgn(\xi) = -1$, if $\xi < 0$). Furthermore, the numerical stability is ensured using satisfactorily smaller time steps ($\Delta t < \Delta t_{critical}$). As mentioned earlier, once the new velocities are computed, the displacement (Δu) and rotation ($\Delta \theta$) increments are obtained (Equation (3)) to calculate the new position of the block centroid (x^{t+}), given in Equation (4). Accordingly, block vertices and edge orientations are determined that are essential to computing contact (interaction) forces.

$$\Delta u = (\dot{u}^{t+})\Delta t \tag{3.1}$$
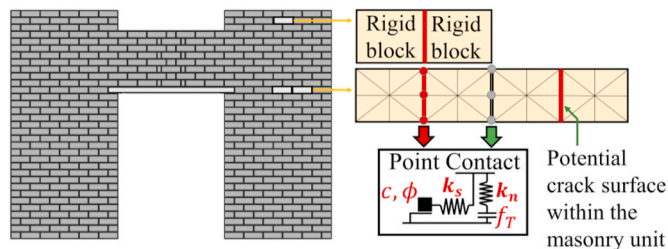
$$\Delta \theta = (\omega^{t+})\Delta t \tag{3.2}$$

Fig. 2. Discrete rigid block model and point contact representation (2D).

$$x^{t+} = x^t + \Delta u \tag{4}$$

The updated spatial configuration of the discontinuous system is utilized to compute new contact forces developing among the adjacent blocks via orthogonal linear/non-linear springs defined at each contact point (see Fig. 2). The employed numerical formulation is based on the soft contact approach, which allows the interpenetration at contact points controlled by the normal (k_n) and shear (k_s) stiffness, as shown in Fig. 2. The relative contact displacement increments are traced through the calculation steps to determine the contact stress increments in the normal ($\Delta\sigma$) and shear ($\Delta\tau$) directions among the adjacent blocks. Also, the elastic contact stress increments are simply obtained as written in Equations (5) and (6).

$$\Delta\sigma = k_n \Delta u_n \tag{5}$$

$$\Delta\tau = k_s \Delta u_s \tag{6}$$

where Δu_n and Δu_s denote the decomposed relative contact displacement in the normal and shear directions, respectively. Then, each stress increment is added to the previous one to obtain the new contact stresses (Equations (7) and (8)), which are later multiplied by the associated contact area to be utilized as forces in equations of motion.

$$\sigma^{t+} = \sigma^t + \Delta\sigma \tag{7}$$

$$\tau^{t+} = \tau^t + \Delta\tau \tag{8}$$

It is worth mentioning that new contact stresses are corrected (if applicable) via a predictor-corrector algorithm, as performed in non-linear explicit numerical solutions. Typically, DEM-based simulations employ rather simpler contact constitutive models and neglect fracture energies associated with cracking and shear failures. Recently, the authors proposed bilinear, polynomial, and exponential fracture energy-based softening constitutive contact models to better capture the post-peak response of brickwork assemblages [29,30]. Similarly, in this study, a bilinear fracture energy-based softening contact model is utilized in tension, shear, and compression, as shown in Fig. 3. It is noted that the Coulomb-slip joint model is used in shear, requiring cohesion (c_0), friction angle (φ_0), mode-II fracture energy (G_f^{II}), residual cohesion (c_{res}) and residual friction angle (φ_{res}), whereas tension and compression behavior are defined considering tensile strength (f_T), mode-I fracture energy (G_f^I) and compression strength (f_C) with associated fracture energy (G_C), respectively. Finally, damage in tension and shear are coupled using a single damage parameter, which is further explained in Pulatsu et al. [45].

The proposed DEM-based modeling framework is performed using 3DEC, a commercial three-dimensional discrete element code developed by ITASCA [46]. The adopted contact models are written in C++ and compiled as DLL (dynamic link library) into 3DEC via the user-defined constitutive model option. In the next section, validation of the proposed modeling strategy is presented, where the in-plane behavior of the URM pier-spandrel system is analyzed.

4. Validation study

In this section, the validation of the proposed D-RBA approach is presented using a previously published experimental study. The computational model is validated using the experimental program performed by Augenti et al. [47].

4.1. Experimental setup

The URM pier-spandrel system used in this study to validate D-RBA was a tuff stone masonry wall with a central opening (Fig. 4a). The masonry was a double-leaf, running bond assemblage of Neapolitan yellow tuff stones ($150 \times 300 \times 100$ mm³ in size) connected with each other through pozzolana-like hydraulic mortar joints which were 10 mm thick. The specimen was made of two equal piers with 1.70 m width and a spandrel with 1 m height, having the masonry above the opening supported by a timber lintel with anchorage length equal to 150 mm within both piers. The central opening was 1.70 m wide, resulting in the same size of piers. Thus, the overall length and height of the specimen were respectively equal to 5.10 m and 3.62 m, whereas the thickness was 0.31 m. Each pier was constructed above a reinforced concrete beam, cast in place, and rigidly anchored to the laboratory basement via Ω-shaped steel plates bolted to squared holes on both sides of the pier.
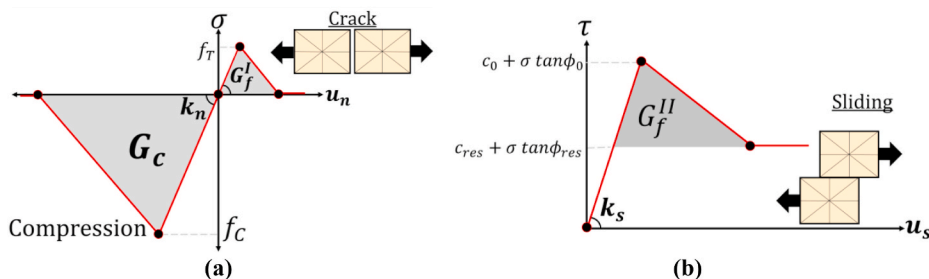

Fig. 3. Contact constitutive law assigned to unit-mortar interface: (**a**) Tension-compression; (**b**) Shear.
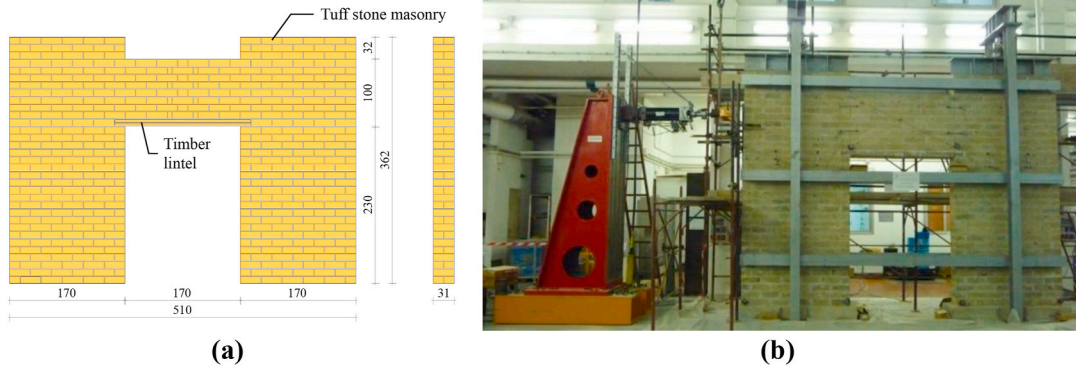
Fig. 4. Experimental setup: (**a**) Geometry of specimen (dimensions in cm); (**b**) Picture of the instrumented specimen before testing.

Vertical forces were applied on top of both piers by means of hydraulic jacks, stiffened steel I-beams with the same width of the piers, and transverse steel portal frames that were fixed to the laboratory basement (Fig. 4b). Each portal frame created a reaction system against the vertical force applied to the pier, whereas the stiffened I-beam allowed a uniform distribution of compressive pressures on the masonry below. On each side of the specimen, three horizontal I-beams beams were bolted to the columns of the portal frames at different heights, ensuring the safety of the technicians (protection against unexpected out-of-plane movements) and further connection of vertical reaction systems. In-plane lateral loading on the specimen was monotonically applied with displacement control through a servo-hydraulic actuator, which was connected to a non-prismatic, stiff reaction wall fixed to the laboratory basement. Shear and flexural deformations were measured using wire potentiometers and linear variable differential transformers (LVDTs). An additional LVDT was installed on the opposite side of the specimen with respect to the servo-hydraulic actuator to measure the lateral displacement experienced by the specimen under lateral loading.

4.2. Numerical simulation of experimental test through D-RBA

The discrete rigid-block model was developed by adopting the identical geometrical properties mentioned in the previous section. Given that the deformations are lumped at the joints, assigned spring stiffness corresponds to the elastic properties of the masonry (i.e., Young's and shear modulus; E and G), which were taken from the benchmark study. Accordingly, the contact stiffness in the normal and shear directions was computed as follows:

$$k_{n,j} = E/h \tag{9.1}$$

$$k_{s,j} = G/h \tag{9.2}$$

where h stands for the vertical joint spacing, approximately 0.1 m. Furthermore, the non-linear contact properties were taken from the comprehensive material testing series reported in related studies [48,49]. For the sake of simplicity, the same strength and stiffness values are used for bed and head joints. The adopted linear and non-linear strength parameters are given in Table 1, in which the tensile, shear, and compressive fracture energies are calculated (if not provided in referred studies) based on the suggestions presented by Lourenço [50].

First, the discrete element model was brought into equilibrium under gravity loads and vertical pressures (corresponding to 200 kN per pier), as indicated in Fig. 5. Then, lateral loading was applied considering relatively low displacement rates (i.e., 0.001 m/s) prescribed at the block center of mass (see Fig. 5 - indicated adjacent to the lateral force). The corresponding reaction forces were computed using a subroutine implemented in the software based on FISH functions, an executable programming language in 3DEC. Note that since the executed explicit solution scheme is prone to numerical oscillations due to abrupt changes in displacements/velocities, the applied displacement rate was kept sufficiently small to obtain smooth and stable results, as discussed in Ref. [26]. In the proposed computational model, the timber lintel was simulated as a deformable block (discretized into finite-difference volumes,

Table 1
Linear and non-linear contact properties.

Interaction within masonry units				
$k_{n,u} (GPa/m)$	$k_{s,u} (GPa/m)$	$f_{t,u}^{*}, c_u (MPa)$	$\theta_{0,u}, \theta_{res}(°)$	$G_{f,u}^{I}, G_{f,u}^{II} (N/m)$
10	4	0.23, 0.46	38, 38	8, 550
Interaction between the masonry units ($\psi = 0°$)				
$k_{n,j} (GPa/m)$	$k_{s,j} (GPa/m)$	$f_{t,j}, c_j^{*} (MPa)$	$\varphi_{0,j} (°)^{*}$	$\theta_{res,j} (°)^{a}$
20	8	0.15	16.2	14.6
$f_C (MPa)^{a}$	$G_{f,u}^{I} (N/m)$	$G_{f,u}^{II} (N/m)^{*}$	$G_C (N/m)$	
3.96	4.3	125	12,800	

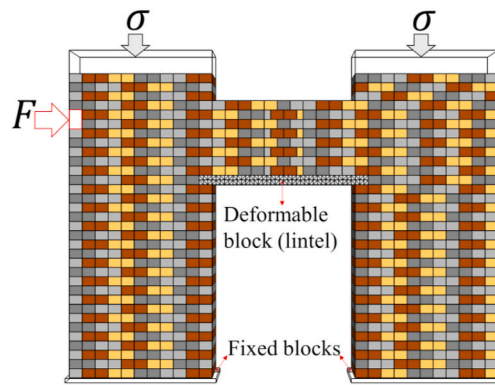[a] *Data taken from experimental studies* [48,49],

Fig. 5. Representation of the discrete element model, including vertical stresses, lateral loading, and boundary conditions.

shown in Fig. 5) with a low bending stiffness, where $E \approx 0.3$ GPa, to better capture both flexural and shear deformations. Even though the lintel-spandrel interaction is an intricate subject deserving further research, the addition of the timber lintel into the computational model is a significant improvement. Observed behavior was better approximated this way because the residual shear strength of
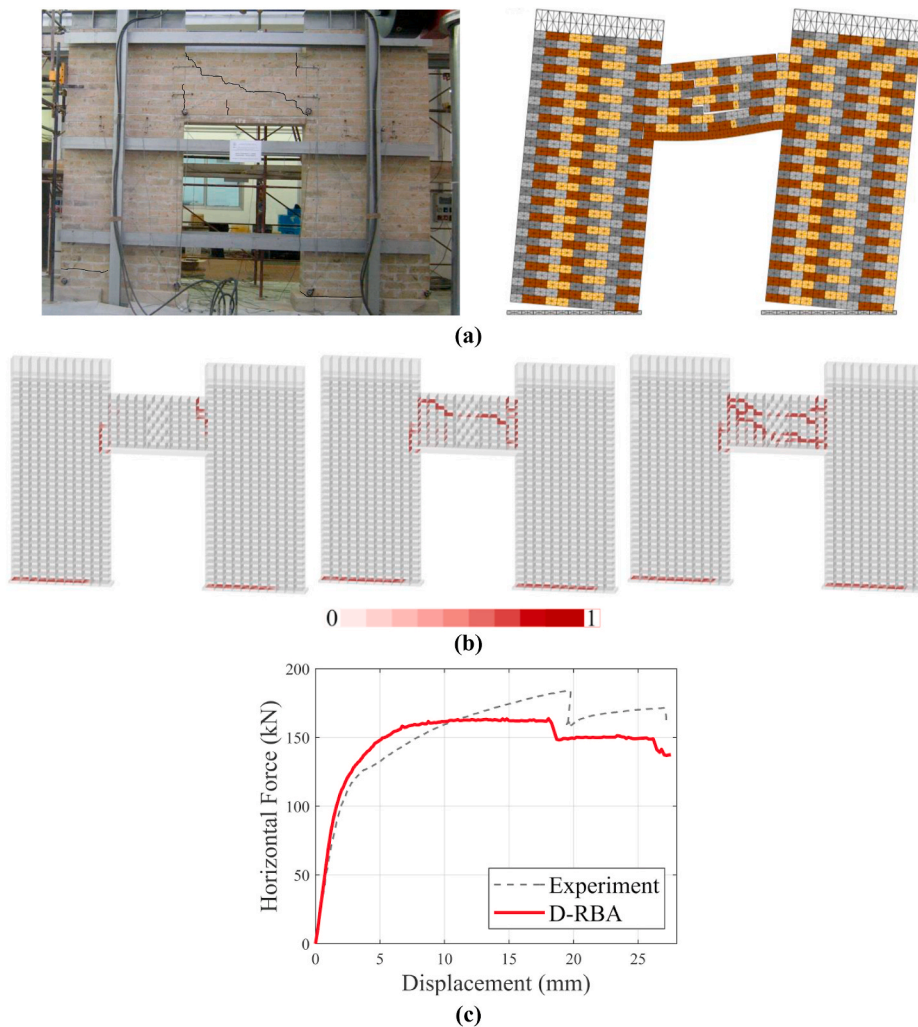

Fig. 6. Comparison between experimental results and results of the proposed D-RBA: (**a**) Experiment (Left); Computational Model (Right) - (**b**) Computational progressive joint opening (corresponding to cracks) under lateral deflections (from left to right); 10, 20 and 30 mm – (**c**) Force vs. displacement curves obtained from experiment and D-RBA.

spandrels is significantly affected by the presence of lintels [12]. Displacement time history was monitored during the analysis for subsequent comparison with experimental findings.

The damage state of the physical testing and discontinuum model are shown in Fig. 6a, which is associated with the maximum displacement imposed during testing (almost 30 mm). As depicted from the explored damage progression (see Fig. 6b), first, flexural cracks developed at the base of the piers and pier-spandrel wall connections, then successive diagonal tensile cracks occurred in the spandrel, as observed during the experiment. In general, the results show that D-RBA captures both pre- and post-peak responses of the URM pier-spandrel system, in line with the experimental results shown in Fig. 6c in terms of the force-displacement diagram. Approximately 10% difference between computational and experimental result regarding the peak base shear is noted. This difference can be attributed to the complexity of the experimental setup (*i.e.*, boundary condition and pre-loading protocol), material uncertainty, and the uniqueness of the testing.

In the next section, the validated computational model is utilized to investigate all possible failure modes of the pier-spandrel system, considering different material properties.

5. Probabilistic D-RBA

Masonry structures are most often analyzed using deterministic methods, even though masonry properties have a probabilistic nature. Such variations stem from the inherent differences of the material properties and uneven deterioration of masonry. In addition, the very same specimen might yield significantly different elastic and inelastic properties depending on the experimental method applied [51]. Probabilistic structural models that account for the uncertainties in material properties and their effects on the strength and behavior of structures are deemed more realistic for structural engineering problems associated with random variables [52]. Probabilistic assessment of masonry structures that considers the uncertainty in the material properties has recently been employed for various structural typologies [21,53–59]. These examples demonstrated the importance of stochastic modeling on capacity and behavior prediction and highlighted the need for substantial research to quantify the uncertainties in the analysis. In this regard, the probabilistic D-RBA analysis carried out in this study considered the uncertainties in material properties, investigating their effects on the capacity and behavior of URM walls with openings.

5.1. Data preparation

Two types of joint and unit properties for masonry were considered in the probabilistic analysis: random and dependent properties. Note that the same elastic stiffness is considered for the lintel during the analyses. The random parameters taken into consideration in this study are the compressive strength of masonry ($f_{c,m}$), the joint (unit-mortar interface) tensile strength ($f_{t,j}$), the tensile strength of units ($f_{t,u}$), the friction angle (φ), and the stiffness ratio R given as the stiffness of units divided by the joint stiffness ($k_{n,u}/ k_{n,j}$), as presented in Table 2. The mean value and coefficient of variation (CoV) of strength parameters are taken from the extensive library compiled from experimental results [22,48,49].

The dependent variables are the ones fully correlated with the random variables, and their mean and CoV are the multiples of the random variables. For example, the cohesion of the unit and joint has the following relation: $c_{unit} = 1.5 f_{t,unit}$ and $c_{bond} = 1.5 f_{t,bond}$, respectively. Similarly, the fracture energies are either taken from the available experimental findings or calculated based on the suggestions presented by Lourenço [50], which are given in Table 2.

Normal distribution was presumed for compressive strength, elastic stiffness, and friction angle parameters, whereas the tensile strength of units and joints were assigned a lognormal distribution, following the pertinent literature [54,56,60–62]. Once the statistical distributions and their parameters are defined, the Latin Hypercube Sampling (LHS) method [63] is utilized to derive sample values for Monte Carlo simulations. With the LHS method, 250 simulations without any correlation between the random parameters were run. Fig. 7 presents the histograms of the sampled values and the probability distributions of the random variables. The number of simulations was determined by observing the change in the average maximum lateral force obtained from the analyses. The average maximum force, in Fig. 8, stabilizes after approximately 80 simulations and starts oscillating around 163 kN after that.

Table 2
Variables, their associated distributions, and parameters.

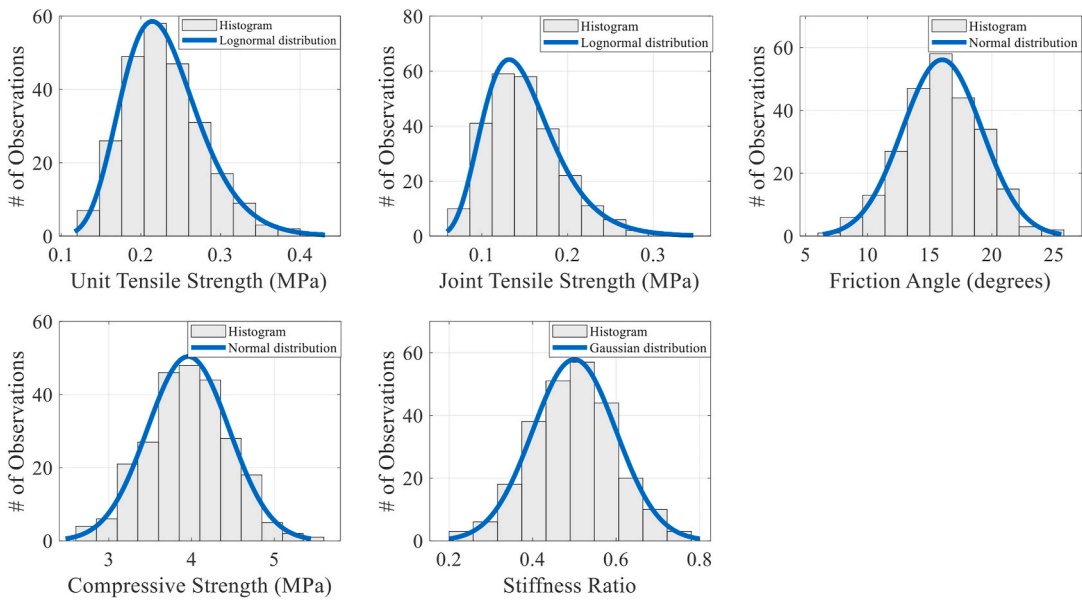| Random Variable	Probability Distribution	Mean (μ)	Coefficient of Variation (CoV)
$f_{c,m}$ (*MPa*)	Normal	3.96	0.125
$f_{t,j}$ (*MPa*)	Lognormal	0.15	0.30
$f_{t,u}$ (*MPa*)	Lognormal	0.23	0.22
φ (*degrees*)	Normal	16	0.20
R ($k_{n,u}/k_{n,j}$)	Normal	0.5	0.20
Dependent Variable	**Relationship**		
c	$1.5 f_{t,j}$		
$G_{f,I}$	$0.029 f_{t,bond}$		
G_C	$3.2 f_m$		

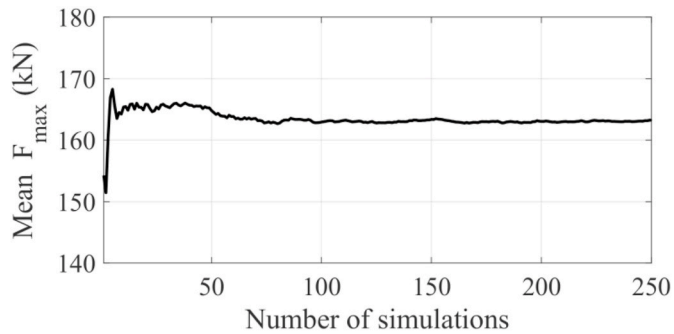**Fig. 7.** Mean estimate of maximum lateral force under varying number of simulations.

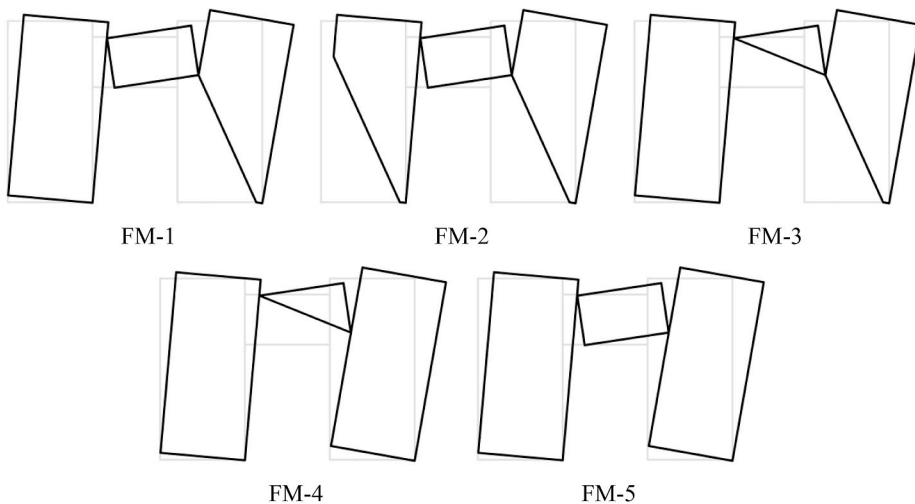**Fig. 8.** Variation of the average maximum lateral force with respect to the number of simulations.

Fig. 9. Distinct failure mechanisms (FMs) of URM pier-spandrel systems.
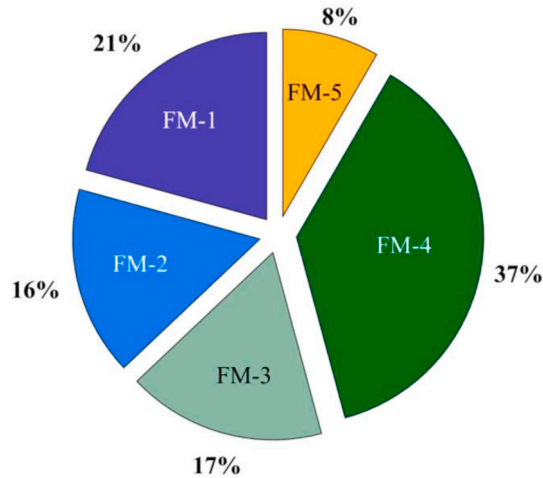
Fig. 10. Pie-chart showing the percentage of the obtained failure modes.

5.2. Distinct failure modes and force-displacement behaviors of the pier-spandrel system

The **non-spatial** probabilistic discontinuum analysis (i.e., each simulation the mechanical properties kept identical spatially within the pier-spandrel system) resulted in five distinct failure mechanisms (FMs) grouped according to their near-collapse behavior, as shown in Fig. 9. The salient feature of these collapse modes is controlled by the sole pier, spandrel, or combined pier-spandrel action. The computational investigations demonstrated that the localized crack patterns are developed mainly at the pier-spandrel connections due to flexural tensile stresses and in the pier and spandrels as diagonal tension cracks. The total number of each failure mechanism among the 250 analyses is shown in Fig. 10.

The first two failure modes, FM-1 and FM-2 (37% of all simulations), correspond to a failure mechanism, which starts as a flexural tensile crack at the pier-spandrel connections and progresses through the piers, causing an eventual mixed-mode failure (i.e., diagonal tensile failure and sliding). Note that while only the right pier suffers from tension and shear damage at the joints in FM-1 (Fig. 11), both piers fail due to diagonal tension in FM2, illustrated in Fig. 12. As can be depicted from examples of force-displacement curves for FM-1 and FM-2 (see Figs. 11a and 12a), diagonal tension cracks in the piers yield abrupt force-drops in the lateral strength of the URM pier-spandrel system, which will be further discussed in the following sections.

In FM-3 and FM-4, flexural tension and shear cracks, developing in the spandrel, become predominant, which constitute 54% of all the simulations. An additional diagonal crack in the piers is noticed for FM-3, while flexural damage at pier toes is observed in both FM-
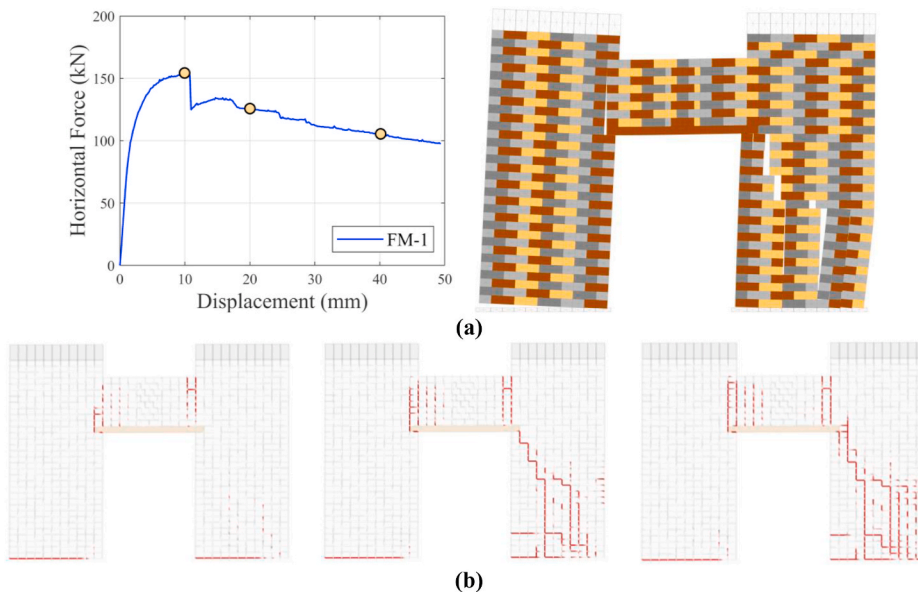

Fig. 11. Illustration of **FM-1**: Typical force-displacement behavior and progressive tensile failure at the joints: (**a**) **Left**: Force vs. displacement response; **Right**: Near-collapse mechanism (computational model) - (**b**) Progressive joint opening (from left to right); 10, 20 and 40 mm.

Fig. 12. Illustration of **FM-2**: Typical force-displacement behavior and progressive tensile failure at the joints: (**a**) **Left**: Force vs. displacement response; **Right**: Near-collapse mechanism (computational model) – (**b**) Progressive joint opening (from left to right); 10, 20 and 40 mm.
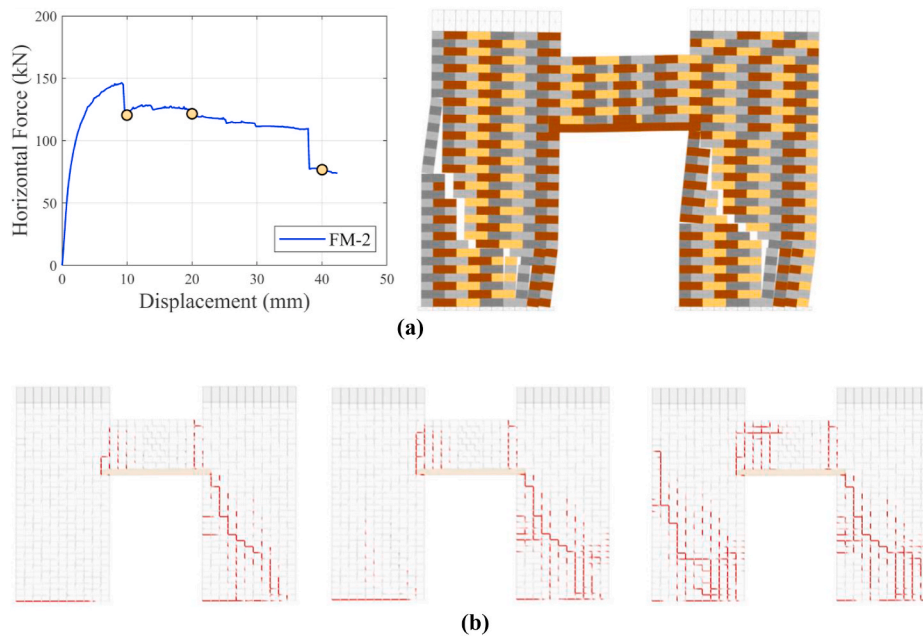
3 and 4. Nonetheless, it is essential to note that both failure mechanisms demonstrate significant ductility and higher strength. A typical force-displacement curve, damage pattern, and the evolution of damage for FM-4, are shown in Fig. 13.

Finally, the rocking behavior of the pier-spandrel system, including flexural cracks along the pier-spandrel connections, is denoted as FM-5 (see Fig. 14). Such a failure mode is associated with the highest lateral resisting force among all failure modes and the ability to maintain that lateral force up to large displacements. Although early flexural cracking of pier-spandrel connections decreases the stiffness, no strength degradation is observed until the toe crushing in the pier, shown in Fig. 14. This failure mode makes up 8% of all simulations, confirming that global rocking mechanisms of URM wall systems representative of old masonry buildings (which was the case considered in the experimental testing campaign, see Sect. 4) rarely occur, but they would provide the best response to in-plane lateral loading as expected for new buildings in seismic design codes.
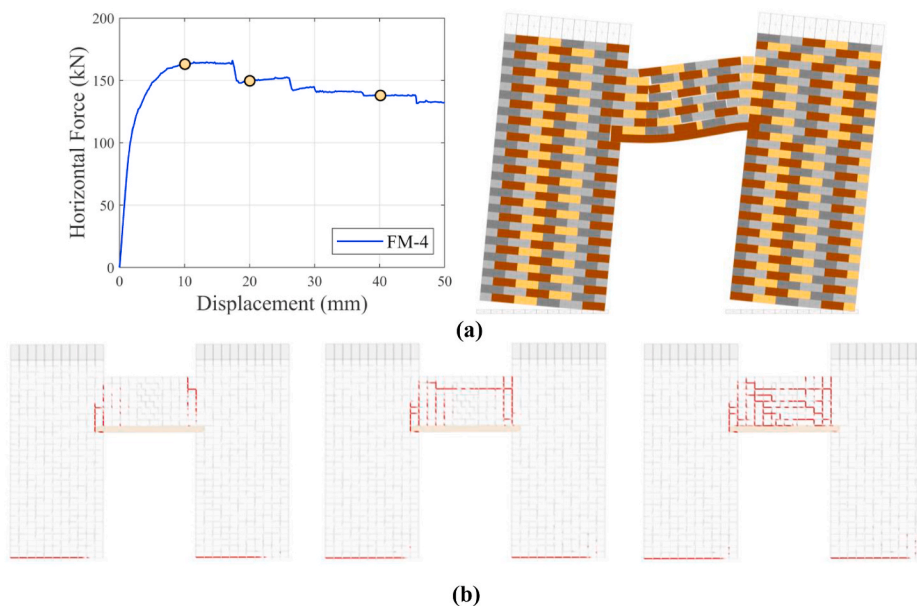

Fig. 13. Illustration of **FM-4**: Typical force-displacement behavior and progressive tensile failure at the joints. (**a**) **Left**: Force vs. displacement response; **Right**: Near-collapse mechanism (computational model) – (**b**) Progressive joint opening (from left to right); 10, 20 and 40 mm.

Fig. 14. Illustration of **FM-5**: Typical force-displacement behavior and progressive tensile failure at the joints: **(a)** Left: Force vs. displacement response; Right: Near-collapse mechanism (computational model) – **(b)** Progressive joint opening (from left to right); 10, 20 and 40 mm.
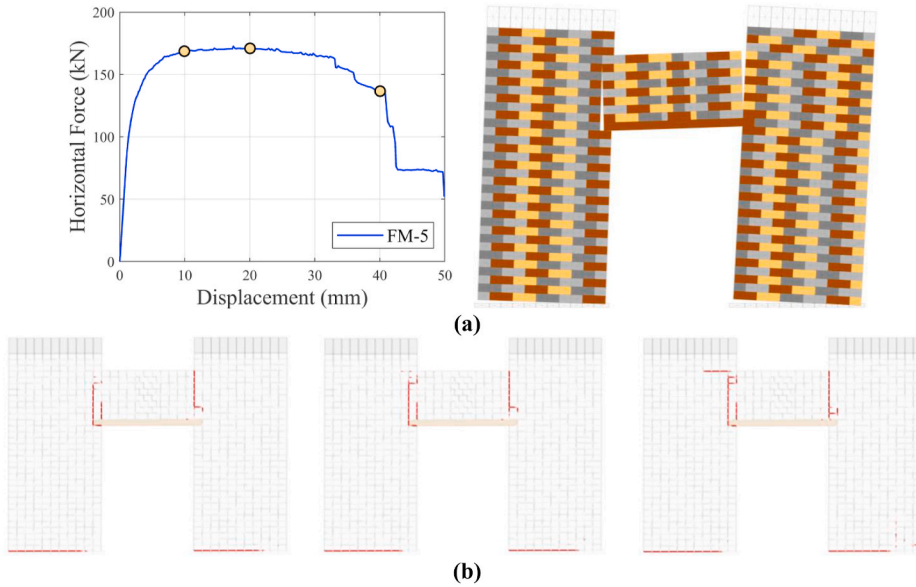
5.3. Interpretation of results considering the influence of material properties

In this section, the previously presented failure modes are further investigated to reveal any correlation between the material properties and the strength or displacement capacity of the pier-spandrel system. Here, the degree of correlation is represented by Pearson product-moment correlation coefficient, $\rho_{x,y}$ (Equation (12)), which quantifies a linear statistical dependence between two random variables (x, y). This correlation coefficient ranges between 0 and 1, which respectively indicates zero and full correlation.

$$\rho_{x,y} = \frac{\Sigma(x_i - \bar{x})(y_i - \bar{y})}{\sqrt{\Sigma(x_i - \bar{x})^2(y_i - \bar{y})^2}} \tag{12}$$

For all failure modes, the correlation between the joint tensile strength and the lateral load capacity of the system is found to be substantial. In contrast, very little or no correlation was found with the other parameters. Fig. 15 not only shows the effect of the joint tensile strength on the load-carrying capacity for each failure mode but also represents how the failure modes change depending on whether the joint tensile strength ($f_{t,j}$) is higher, or lower than its mean value. According to the results of the analyses, FM-3 and FM-4 are almost directly correlated with the system's load carrying capacity, as the correlation coefficient reaches unity. For other failure modes, the correlation is still significant. FM-1 and FM-2 are associated with low $f_{t,j}$, whereas FM-3, FM-4, and especially FM-5 have higher $f_{t,j}$. This result emphasizes that the joint tensile strength governs the in-plane lateral resistance of the system; and hence, the associated collapse mechanism. However, it would be better to be cautious at this point since it may also be overlooking the effects of
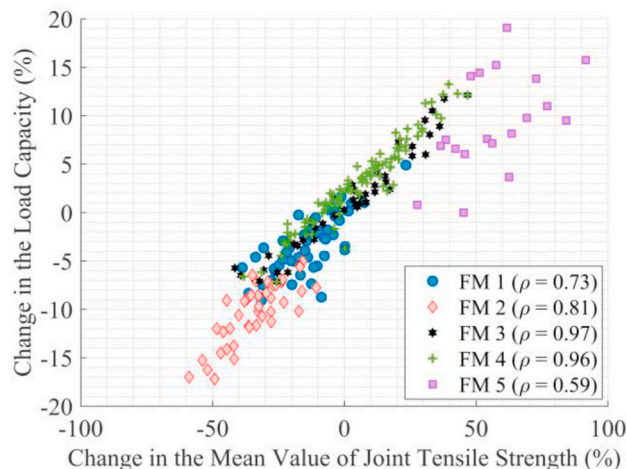

Fig. 15. Influence of the joint tensile strength on the lateral load capacity of the pier-spandrel system.
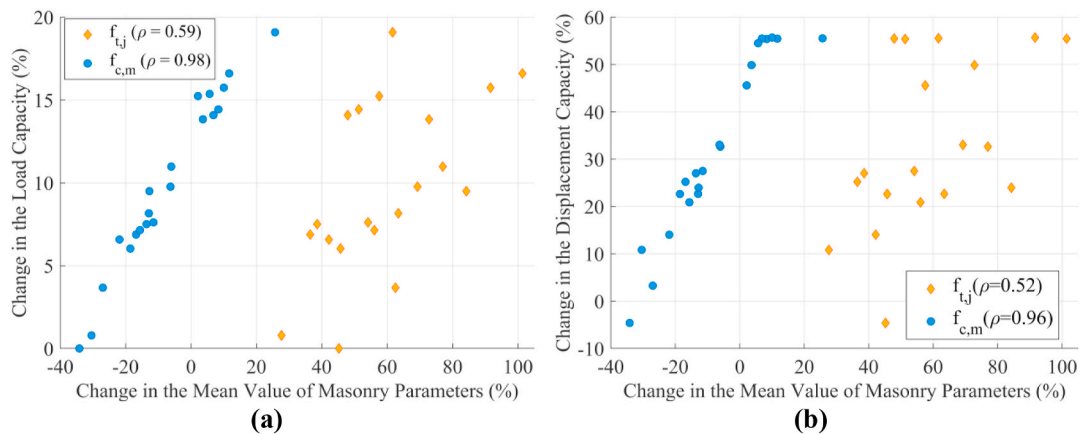
Fig. 16. Percent change in the load and displacement capacity of the pier-spandrel system for the joint tensile strength and compressive strength of masonry – FM5: (**a**) Load – (**b**) Displacement Capacity.

joint friction angle due to specified vertical stress and boundary conditions, as the joint friction angle was found to be very influential on the lateral resistance of single URM walls in previous studies [10,35,54,64]. In addition, the load-carrying capacity of the system is found to be correlated above 95% with compressive strength for FM-5. This observation also makes sense as compression failure of the pier occurs in FM-5. It is important to note that toe crushing was observed during testing, effectively simulated via the proposed non-linear modeling strategy.

In terms of correlation among material properties and the displacement capacity of the pier-spandrel system, no inference could be made except for FM-5. As illustrated in Fig. 16, only FM-5 provides correlations between the displacement capacity and the joint tensile strength, and the compressive strength of masonry.

6. Simplified macro block analysis vs. DRBA

In this section, the two most obtained failure modes (FM-1 and FM-4) are revisited and analyzed according to the displacement-based approach defined by the Italian building code [65]. In contrast to the classical force-displacement approach [66], which only provides the load multiplier that activates the failure mechanism, the displacement-based approach considers varied kinematic configurations to evaluate the curve descending branch [67,68,69].

The analyses involve as parent mechanisms both FM-1 and FM-4 that are investigated under different hypotheses, i.e., considering infinite or finite compressive strength of the masonry. According to Refs. [70,71], when infinite compressive strength is considered, the interface is called impenetrable, and the hinges (centres of rotation) can form only at the end-points of the interface, as shown in Fig. 17a. On the other hand, when the compressive strength of the masonry is finite, crushing occurs, and a suitable model should be used to schematize the crushing phenomenon, revealed in Fig. 17b. Thus, the position of the hinge must be moved over a distance t_h that defines the resultant location of the constant compressive stress at the interface between the macroblock and the support (see Fig. 17b). It is computed by equating the resultant of the rectangular compressive stress with the total axial load actions that reads:

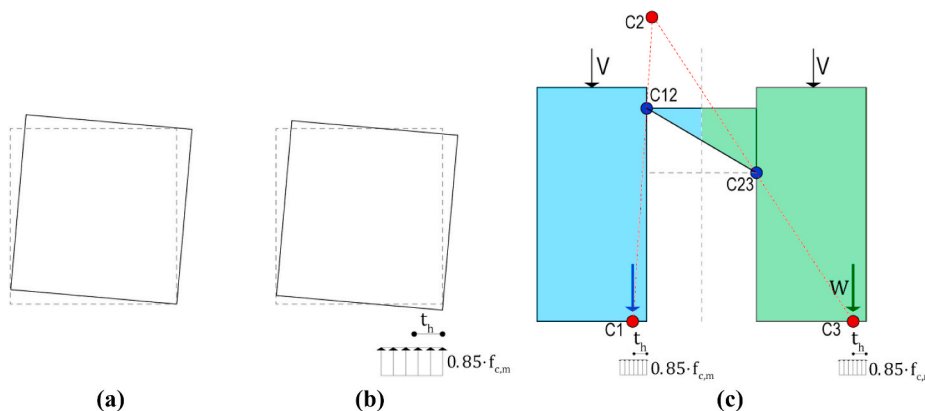$$t_h = \frac{\Sigma W_i}{2 \cdot 0.85 \cdot f_{c,m} \cdot t} \tag{13}$$

Fig. 17. (**a**) Kinematic of the single block: infinite compressive strength; (**b**) kinematic of the single block: finite compressive strength; (**c**) kinematic of FM-4: finite compressive strength.

where W_i are the vertical forces arising from the self-weight and the dead load acting of the top of the spandrel, t is the thickness of the wall and $f_{c,m}$ is the compressive strength of the masonry. The Italian standard [65] suggests this formulation in particular when the mechanism involves only one macroblock, and thus the kinematic chain has only an external hinge connected to the ground. In order to apply such formulation for a pier-spandrel system, i.e., a system constituted by three parts having two rotational hinges constrained to the ground and two internal hinges, it is required to consider an additional hypothesis that consists in distributing the axial vertical loads to the hinges C1 and C3. The axial actions are measured according to the influence area defined from the mid-axis that passes from the spandrel to the left or right edge for the hinge C1 and C3, respectively. As illustrated in Fig. 17c, rotational hinges C1 and C3 are slightly moved of a quantity t_h.

A further hypothesis is to consider the position of the internal hinges, namely C12 and C23, not coincident with the corner but slightly moved to consider the crushing of the masonry in those locations (see Fig. 18). To this end, a further configuration has been considered, i.e., Macro-Block 2, just by moving the position of the hinges C12 and C23 below and above, respectively, of a distance equal to one block height. The adopted kinematic configurations are summarized in Fig. 18.

The considered kinematic configurations (FM-1 and FM-4) may be described by adopting only one degree of freedom, even though three parts form the kinematic chain. As a consequence, the virtual rotation of each block may be defined by multiplying a constant for the chosen degree of freedom, where the constants are computed by respecting geometrical compatibility rules. Once the kinematic of each part is mathematically defined, the principle of the virtual work may be adopted to calculate the value of the horizontal force that guarantees the equilibrium between stabilizing and destabilizing work.
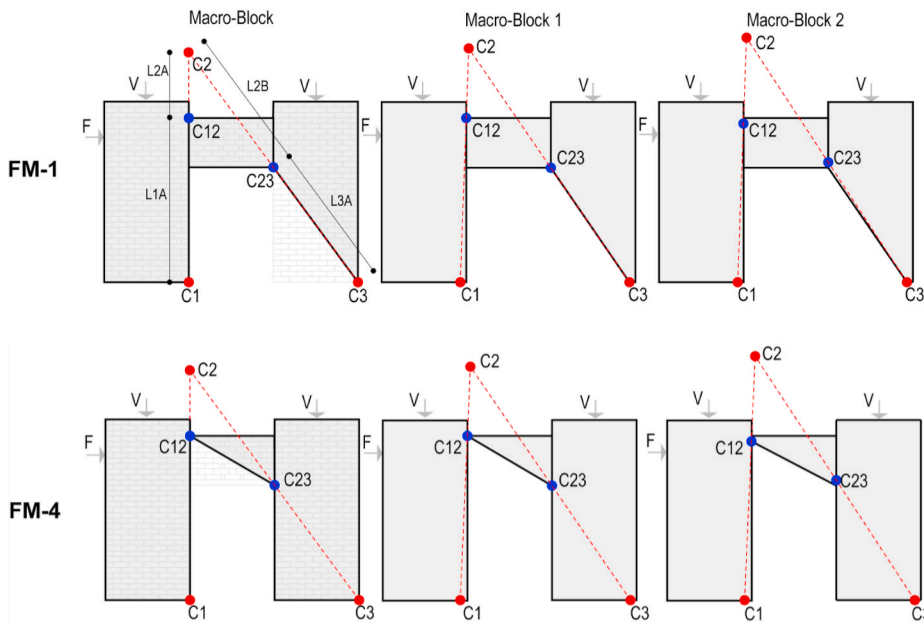

Fig. 18. Kinematic chains of the investigated failure mechanisms (FM-1 and FM-4).
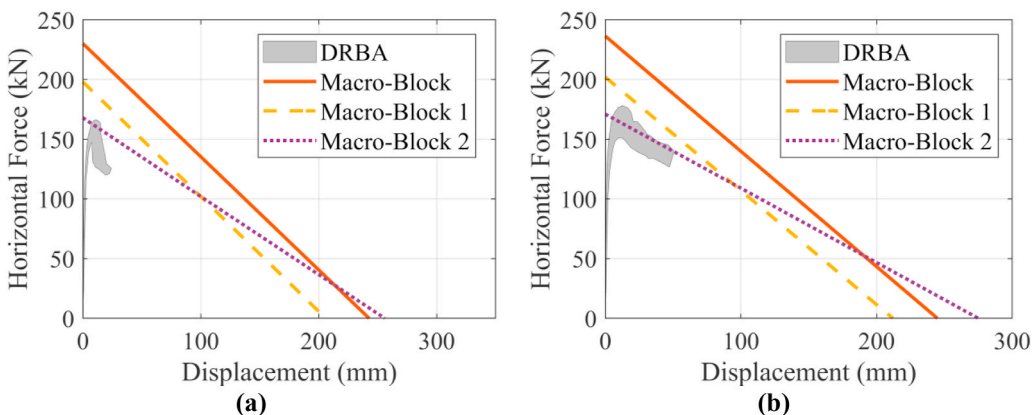

Fig. 19. Comparison of different macro-block solutions and overall (envelope) D-RBA for two failure mechanisms: **(a)** FM-1 and **(b)** FM-4.

Thus, such an approach is adopted for varied kinematic configurations to evaluate the curve descending branch by using as a control point the place where is applied the horizontal force. Fig. 19 reveals the comparison of three macro-block configurations and an envelope of the DRBA. While the results obtained from infinite crushing strength in macro-block representation overshoot the capacity of the analyzed masonry pier-spandrel system, macro block-1 and macro block-2 configurations (including limited compressive strength and modified hinge locations) provide similar results with DRBA for both failure mechanisms, FM-1, and FM-4 (see Fig. 19). This outcome exemplifies that simplified solutions can be refined and practically modified in the light of advanced modeling techniques, suggesting a compromise among the employed computations.

7. Discussion on collapse mechanisms and drift limits

Post-earthquake reconnaissance and experimental results have shown three distinct behavior patterns for spandrels: (*i*) shear cracks forming due to shear dominated behavior of the spandrel, (*ii*) flexural cracks observed as nearly vertical cracks due to bending of piers, and (*iii*) a combination of these two types, also called mixed-type behavior [16]. The distinct failure mechanisms obtained through the probabilistic analysis highlight the complexity of the problem and the piers-spandrel interaction. Both piers and spandrels contribute to the stiffness, strength, and macro-behavior of the pier-spandrel system, making it difficult to predict the failure mode of a pier-spandrel system under seismic loading.

In Fig. 20, force-displacement curves for 250 simulations are presented. Specifically, Fig. 20a shows full curves, where the lateral forces are applied up to 50 mm displacement, whereas, in Fig. 20b, the same force-displacement curves are truncated at 80% of the maximum lateral force once the degradation has started. It is evident that the ultimate displacement capacity can be remarkably different based on the decision where the post-peak strength value is determined. The ultimate deformation capacity of URM walls is generally defined as the point at which the strength drops to 80% of its value [13]. For most spandrel configurations, however, the decrease in lateral strength exceeds 20% after attaining the peak strength, but spandrel could sustain higher deformations without the complete loss of load carrying capacity. Therefore, if the same definition is applied to the spandrels to determine their ultimate displacement, it would be a conservative assumption, and we may underestimate the deformation capacity. In this regard, the residual shear strength of masonry spandrels is explicitly taken into account in various standards. It might be presumed that all failure modes are significantly affected by the constraint on the ultimate displacement, as shown in Table 3, confirming Beyer's remark in Ref. [13]. Furthermore, for all failure modes (FM-1 to 5), the coefficient of variation of the peak lateral resisting force is less than or equal to 5%. On the other hand, the ultimate displacements (considered at $0.8F_{max}$) have significantly higher CoV, ranging between 16 and 32%, which highlights the noticeable variation in the displacement capacities.

The first and second failure mechanisms represent weak pier-strong spandrel systems, which yield premature collapse at relatively small lateral deformations (hence drift ratios). As shown in Fig. 21, FM-1 and FM-2 result in lower strength and displacement capacities
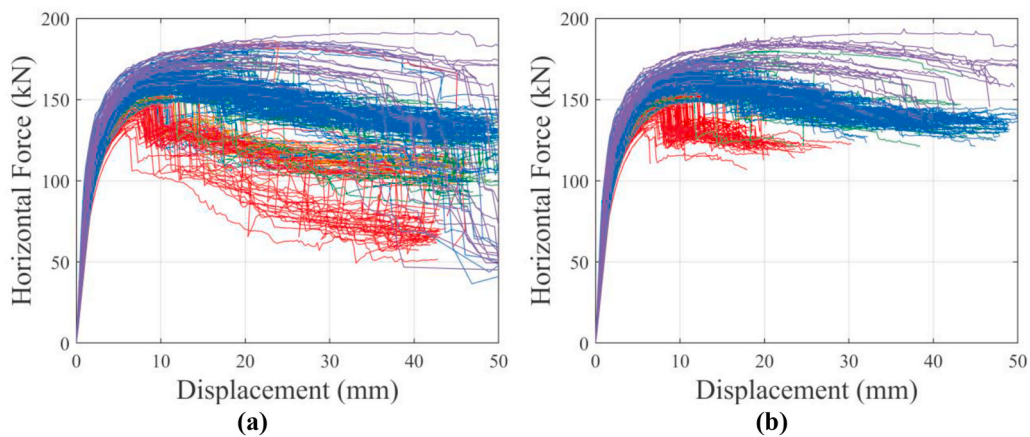

Fig. 20. All force-displacement curves: (**a**) complete behavior, (**b**) curves truncated at $0.8F_{max}$.

Table 3
Average maximum force and displacement for each failure mode.

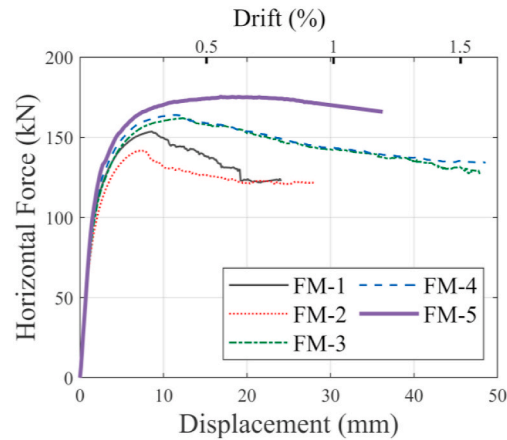|		FM1	FM2	FM3	FM4	FM5	All Data
F_{max}	Mean (kN)	157.6	146.5	165.3	168.3	179.5	163.25
	CoV	0.03	0.04	0.05	0.04	0.05	0.07
D_{max}	Mean (mm)	44.7	42.2	48.8	48.8	50.0	47.30
	CoV	0.05	0.05	0.05	0.07	0.02	0.09
D_{max} @ 0.8 F_{max}	Mean (mm)	16.3	18.5	36.2	41.9	42.6	32.11
	CoV	0.25	0.32	0.26	0.17	0.16	0.43

Fig. 21. Moving average of the lateral force vs. drift curves for each failure mode.

compared to others. Therefore, they can be grouped as pier failure, where diagonal tensile cracks accompanied by flexural failure of the piers control these two failure modes, and the ultimate drifts are between 0.8 and 1%. These ultimate drifts are in line with the drift limits given in many structural codes, even though stone masonry is not in the scope of such standards. FM-3 and FM-4 can be grouped as the mixed-type failure of the spandrel, including shear and flexural cracks. Due to the initial rotation of the piers, flexural cracks develop first. As the axial force increases due to the increasing deformations, shear cracks form due to a diagonal compression strut, and the shear behavior controls the residual strength. It is seen that these failure modes have the highest ductility and drift capacity (>1.5%), making it a satisfactory behavior sought during seismic events. Finally, FM-5 is a combination of flexural spandrel failure and excessive rotations of the piers causing toe crushing. That behavior mode is associated with the highest strength and a significant drift capacity, over 1%, which agrees well with Italian code assumptions on masonry structures in case of flexural failure. It is important to note that in Fig. 21, the moving average (i.e., the average of forces corresponding to each data point on the displacement axis) is used to show the force-displacement curves, whereas, in Table 3, the mean values of the maximum displacement are considered.

8. Conclusions

This research presents an alternative discontinuum-based computational modeling framework to simulate unreinforced masonry systems considering material uncertainties based on the discrete element method. Particularly, the nonlinear behavior of URM pier-spandrel systems under lateral forces and the mechanical properties affecting the behavior are investigated. The proposed modeling strategy captures experimentally observed damage patterns and replicates the force-displacement relationship of the pier-spandrel systems. Rigid blocks are used to replicate the URM skeleton, and non-linear material laws are implemented at the joints through fracture energy-based contact constitutive models. The accuracy and computational efficiency of the proposed modeling approach enabled conducting probabilistic discontinuum analysis incorporating uncertainties in material properties. A total of 250 Monte Carlo simulations yielded various failure modes that occurred due to shear cracks in the piers, flexural and/or shear cracking of the spandrel, or a combination of both. Out of the five failure modes presented, the first two (denoted as FM-1 and FM-2) consist of pier failure and flexural cracks in the spandrel, resulting in the lowest strength and displacement capacities amongst all. Another couple of failure modes (FM-3 and FM-4) are associated with a mixed-type spandrel behavior characterized by both flexural and shear cracks. Those two failure modes show satisfactory behavior of the pier-spandrel system under in-plane lateral loading with a ductile response and considerable lateral strength. The last failure mode, FM-5, consists of the rocking behavior of the piers and the flexural tensile cracks at the pier-spandrel connections, highlighting the inevitable collapse of the wall system due to toe crushing at the base of the piers. The variability of the failure modes for this specific set-up calls attention to considering the material uncertainty in computational modeling.

The results show that the joint tensile strength of masonry considerably affects the failure type and capacity. In contrast, negligible or no correlation is obtained for other parameters (demonstrated through the reference URM wall system, given its geometric features and boundary conditions (restraints and forces)). Specifically for FM-5, the influence of the masonry compressive strength is found to be highly correlated with the lateral strength and displacement capacity of the pier-spandrel system. FM-3 and FM-4 provide the highest ultimate displacements in terms of drift ratios, whereas relatively more brittle and sudden collapse mechanisms are noted for FM-1 and FM-2, indicating lower drift ratios than the other failure mechanisms. The results clearly show the full picture of the possible collapse mechanisms of URM pier-spandrel systems and underline the lack of deformation capacities of weak-pier strong-spandrel systems, which should be avoided to mitigate seismic vulnerability.

Additionally, practical macro-block configurations are presented to compare against discontinuum-based solutions. It is worth underlining how the simplified macro-block approach tends to match the DRBA results, suggesting the adoption of a macro-block model able to take into account the crushing phenomenon of both internal and external hinges. This outcome exhibits a potential bridge between the practical calculations and advanced models, where observations derived in the latter may help prepare a refined simplified solution.

The results of this study may be limited to the examined pier-spandrel system. Thus, similar studies are recommended for various lintel types (*e.g.*, arch, reinforced concrete, timber, etc.). A detailed discussion regarding the floor slab – spandrel wall interactions would also be beneficial. Additionally, future studies may focus on the change in vertical stress levels and the geometry of the system, such as the number of piers or the aspect ratios of the spandrel and piers. Finally, probabilistic analysis of such systems can be investigated to account for the spatial variability of the masonry properties.

Authorship statement

Bora Pulatsu: Conceptualization, software, methodology, validation, analysis, writing – original draft, Semih Gonen: Conceptualization, methodology, data curation, conceptualization, writing – review and editing, Fulvio Parisi: Conceptualization, data curation, resources, writing – review and editing, Ece Erdogmus: Supervision, writing – review and editing, funding acquisition, Kagan Tuncay: Methodology, supervision, writing – review and editing, Marco Francesco Funari: Conceptualization, methodology, writing – review and editing, Paulo B. Lourenco: Supervision, conceptualization, writing – review and editing.

Declaration of competing interest

The authors declare that they have no known competing financial interests or personal relationships that could have appeared to influence the work reported in this paper.

Data availability

Data will be made available on request.

References

[1] A. Shabani, M. Kioumarsi, M. Zucconi, State of the art of simplified analytical methods for seismic vulnerability assessment of unreinforced masonry buildings, Eng. Struct. 239 (2021), 112280, https://doi.org/10.1016/j.engstruct.2021.112280.

[2] S. Akkar, A. Aldemir, A. Askan, S. Bakir, E. Canbay, I.O. Demirel, et al., 8 March 2010 elaziǧ-kovancilar (Turkey) Earthquake: observations on ground motions and building damage, Seismol Res. Lett. 82 (2011) 42–58, https://doi.org/10.1785/gssrl.82.1.42.

[3] G. Vlachakis, E. Vlachaki, P.B. Lourenço, Learning from failure: damage and failure of masonry structures, after the 2017 Lesvos earthquake (Greece), Eng. Fail. Anal. 117 (2020), 104803, https://doi.org/10.1016/j.engfailanal.2020.104803.

[4] A. Aldemir, E. Guvenir, M. Sahmaran, Rapid screening method for the determination of regional risk distribution of masonry structures, Struct. Saf. 85 (2020), 101959, https://doi.org/10.1016/j.strusafe.2020.101959.

[5] F. Parisi, N. Augenti, Earthquake damages to cultural heritage constructions and simplified assessment of artworks, Eng. Fail. Anal. 34 (2013) 735–760, https://doi.org/10.1016/j.engfailanal.2013.01.005.

[6] T. Celano, L.U. Argiento, F. Ceroni, C. Casapulla, Literature review of the in-plane behavior of masonry walls: theoretical vs. Experimental results, Materials 14 (2021) 3063, https://doi.org/10.3390/ma14113063.

[7] P.B. Lourenço, D.V. Oliveira, P. Roca, A. Orduña, Dry joint stone masonry walls subjected to in-plane combined loading, J. Struct. Eng. 131 (2005) 1665–1673, https://doi.org/10.1061/(asce)0733-9445, 2005)131:11(1665).

[8] B. Pulatsu, E.M. Bretas, P.B. Lourenço, Discrete element modeling of masonry structures: validation and application, Earthquakes Struct 11 (2016) 563–582, https://doi.org/10.12989/eas.2016.11.4.563.

[9] D. Malomo, M.J. DeJong, A. Penna, Influence of bond pattern on the in-plane behavior of URM piers, Int. J. Architect. Herit. (2019) 1–20, https://doi.org/10.1080/15583058.2019.1702738, 00.

[10] S. Gonen, B. Pulatsu, S. Soyoz, E. Erdogmus, Stochastic discontinuum analysis of unreinforced masonry walls: lateral capacity and performance assessments, Eng. Struct. 238 (2021), 112175, https://doi.org/10.1016/j.engstruct.2021.112175.

[11] B. Pulatsu, F. Gencer, E. Erdogmus, Study of the effect of construction techniques on the seismic capacity of ancient dry-joint masonry towers through DEM, Eur J Environ Civ Eng (2020) 1–18, https://doi.org/10.1080/19648189.2020.1824823, 0.

[12] K. Beyer, S. Mangalathu, Review of strength models for masonry spandrels, Bull. Earthq. Eng. 11 (2013) 521–542, https://doi.org/10.1007/s10518-012-9394-3.

[13] K. Beyer, Peak and residual strengths of brick masonry spandrels, Eng. Struct. 41 (2012) 533–547, https://doi.org/10.1016/j.engstruct.2012.03.015.

[14] K. Beyer, S. Mangalathu, Numerical study on the peak strength of masonry spandrels with arches, J. Earthq. Eng. 18 (2014) 169–186, https://doi.org/10.1080/13632469.2013.851047.

[15] G. Rinaldin, C. Amadio, N. Gattesco, Review of experimental cyclic tests on unreinforced and strengthened masonry spandrels and numerical modelling of their cyclic behaviour, Eng. Struct. 132 (2017) 609–623, https://doi.org/10.1016/j.engstruct.2016.11.063.

[16] K. Beyer, A. Dazio, Quasi-static cyclic tests on masonry spandrels, Earthq. Spectra 28 (2012) 907–929, https://doi.org/10.1193/1.4000063.

[17] P. Foraboschi, Coupling effect between masonry spandrels and piers, Mater. Struct. Constr. 42 (2009) 279–300, https://doi.org/10.1617/s11527-008-9405-7.

[18] M.K. Howlader, M.J. Masia, M.C. Griffith, Numerical analysis and parametric study of unreinforced masonry walls with arch openings under lateral in-plane loading, Eng. Struct. 208 (2020) 110337, https://doi.org/10.1016/j.engstruct.2020.110337.

[19] Z. Liu, A. Crewe, Effects of size and position of openings on in - plane capacity of unreinforced masonry walls, Bull. Earthq. Eng. (2020), https://doi.org/10.1007/s10518-020-00894-0.

[20] F. Parisi, G.P. Lignola, N. Augenti, A. Prota, G. Manfredi, Rocking response assessment of in-plane laterally-loaded masonry walls with openings, Eng. Struct. 56 (2013) 1234–1248, https://doi.org/10.1016/j.engstruct.2013.06.041.

[21] L.J. Gooch, M.J. Masia, M.G. Stewart, Application of stochastic numerical analyses in the assessment of spatially variable unreinforced masonry walls subjected to in-plane shear loading, Eng. Struct. 235 (2021), 112095, https://doi.org/10.1016/j.engstruct.2021.112095.

[22] F. Parisi, N. Augenti, A. Prota, Implications of the spandrel type on the lateral behavior of unreinforced masonry walls, Earthq. Eng. Struct. Dynam. 43 (2014) 1867–1887, https://doi.org/10.1002/eqe.2441.

[23] R. Nowak, R. Orłowicz, Testing of chosen masonry arched lintels, Int. J. Architect. Herit. (2020) 1–15, https://doi.org/10.1080/15583058.2020.1735573, 00.

[24] D. Malomo, M.J. DeJong, A Macro-Distinct Element Model (M-DEM) for simulating the in-plane cyclic behavior of URM structures, Eng. Struct. 227 (2021), 111428, https://doi.org/10.1016/j.engstruct.2020.111428.

[25] D. Malomo, M.J. DeJong, A Macro-Distinct Element Model (M-DEM) for out-of-plane analysis of unreinforced masonry structures, Eng. Struct. 244 (2021), 112754, https://doi.org/10.1016/j.engstruct.2021.112754.

[26] B. Pulatsu, E. Erdogmus, P.B. Lourenço, J.V. Lemos, K. Tuncay, Simulation of the in-plane structural behavior of unreinforced masonry walls and buildings using DEM, Structures 27 (2020) 2274–2287, https://doi.org/10.1016/j.istruc.2020.08.026.

[27] V. Sarhosis, P. Asteris, T. Wang, W. Hu, Y. Han, On the stability of colonnade structural systems under static and dynamic loading conditions, Bull. Earthq. Eng. 14 (2016) 1131–1152, https://doi.org/10.1007/s10518-016-9881-z.

[28] J.V. Lemos, Discrete element modeling of the seismic behavior of masonry construction, Buildings 9 (2019) 43, https://doi.org/10.3390/buildings9020043.

[29] B. Pulatsu, E. Erdogmus, P.B. Lourenço, J.V. Lemos, J. Hazzard, Discontinuum analysis of the fracture mechanism in masonry prisms and wallettes via discrete element method, Meccanica 55 (2020) 505–523, https://doi.org/10.1007/s11012-020-01133-1.

[30] B. Pulatsu, E. Erdogmus, P.B. Lourenço, R. Quey, Simulation of uniaxial tensile behavior of quasi-brittle materials using softening contact models in DEM, Int. J. Fract. 217 (2019) 105–125, https://doi.org/10.1007/s10704-019-00373-x.

[31] E.M. Bretas, J.V. Lemos, P.B. Lourenço, A DEM based tool for the safety analysis of masonry gravity dams, Eng. Struct. 59 (2014) 248–260, https://doi.org/10.1016/j.engstruct.2013.10.044.

[32] A. Pappas, D. D'Ayala, D.T. Dassanayake, A. Antonini, A. Raby, Rocking of offshore lighthouses under extreme wave impacts: limit analysis, analytic formulations and distinct element method, Eng. Struct. 228 (2021), 111534, https://doi.org/10.1016/j.engstruct.2020.111534.

[33] V. Sarhosis, J.V. Lemos, A detailed micro-modelling approach for the structural analysis of masonry assemblages, Comput. Struct. 206 (2018) 66–81, https://doi.org/10.1016/j.compstruc.2018.06.003.

[34] P.B. Lourenço, J.G. Rots, Multisurface interface model for analysis of masonry structures, J. Eng. Mech. 123 (1997) 660–668.

[35] S. Gonen, B. Pulatsu, E. Erdogmus, E. Karaesmen, E. Karaesmen, Quasi-static nonlinear seismic assessment of a fourth century A.D. Roman aqueduct in istanbul, Turkey, Heritage 4 (2021) 401–421, https://doi.org/10.3390/heritage4010025.

[36] V. Sarhosis, Y. Sheng, Identification of material parameters for low bond strength masonry, Eng. Struct. 60 (2014) 100–110, https://doi.org/10.1016/j.engstruct.2013.12.013.

[37] A. Furukawa, R. Spence, Y. Ohta, E. So, Analytical study on vulnerability functions for casualty estimation in the collapse of adobe buildings induced by earthquake, Bull. Earthq. Eng. 8 (2010) 451–479, https://doi.org/10.1007/s10518-009-9156-z.

[38] A. Rafiee, M. Vinches, C. Bohatier, Modelling and analysis of the Nîmes arena and the Arles aqueduct subjected to a seismic loading, using the Non-Smooth Contact Dynamics method, Eng. Struct. 30 (2008) 3457–3467, https://doi.org/10.1016/j.engstruct.2008.05.018.

[39] A. Ferrante, F. Clementi, G. Milani, Advanced numerical analyses by the Non-Smooth Contact Dynamics method of an ancient masonry bell tower, Math. Methods Appl. Sci. (2020), https://doi.org/10.1002/mma.6113, 7706–25.

[40] H. Smoljanović, N. Živaljić, Nikolić Ž, A. Munjiza, Numerical model for confined masonry structures based on finite discrete element method, Int. J. Eng. Model. 30 (2017) 19–35.

[41] H. Smoljanović, N. Živaljić, Nikolić Ž, A combined finite-discrete element analysis of dry stone masonry structures, Eng. Struct. 52 (2013) 89–100, https://doi.org/10.1016/j.engstruct.2013.02.010.

[42] P.A. Cundall, A computer model for simulating progressive, large-scale movements in blocky rock systems, Int. Symp. Rock Mech. 2 (1971) 47–65. Nancy.

[43] R. Hart, P.A. Cundall, J.V. Lemos, Formulation of a three-dimensional distinct element model - Part II. Mechanical calculations for motion, Int J Rock Mech Min Sci Geomech 25 (1988) 117–125.

[44] P.A. Cundall, C. Detournay, Dynamic relaxation applied to continuum and discontinuum numerical models in geomechanics, in: Rock Mech. Eng., CRC Press, 2017, pp. 57–102.

[45] B. Pulatsu, S. Gonen, E. Erdogmus, P.B. Lourenço, J.V. Lemos, R. Prakash, In-plane structural performance of dry-joint stone masonry Walls: a spatial and non-spatial stochastic discontinuum analysis, Eng. Struct. 242 (2021), 112620, https://doi.org/10.1016/j.engstruct.2021.112620.

[46] Itasca Consulting Group Inc, 3DEC Three Dimensional Distinct Element Code, 2013.

[47] N. Augenti, F. Parisi, A. Prota, G. Manfredi, In-plane lateral response of a full-scale masonry subassemblage with and without an inorganic matrix-grid strengthening system, J. Compos. Construct. 15 (2011) 578–590, https://doi.org/10.1061/(ASCE)CC.1943-5614.0000193.

[48] N. Augenti, F. Parisi, Constitutive modelling of tuff masonry in direct shear, Construct. Build. Mater. 25 (2011) 1612–1620, https://doi.org/10.1016/j.conbuildmat.2010.10.002.

[49] N. Augenti, F. Parisi, Constitutive models for tuff masonry under uniaxial compression, J. Mater. Civ. Eng. 22 (2010) 1102–1111, https://doi.org/10.1061/(ASCE)MT.1943-5533.0000119.

[50] P.B. Lourenço, Recent advances in masonry structures: micromodelling and homogenisation, in: Multiscale Modeling in Solid Mechanics: Computational Approaches. Multiscale Model, solid Mech. Comput. approaches, 2009, pp. 251–294.

[51] S. Gonen, S. Soyoz, Investigations on the elasticity modulus of stone masonry, Structures 30 (2021) 378–389, https://doi.org/10.1016/j.istruc.2021.01.035.

[52] E. Vanmarcke, M. Shinozuka, S. Nakagiri, G.I. Schuëller, M. Grigoriu, Random fields and stochastic finite elements, Struct. Saf. 3 (1986) 143–166, https://doi.org/10.1016/0167-4730(86)90002-0.

[53] J. Park, P. Towashiraporn, J.I. Craig, B.J. Goodno, Seismic fragility analysis of low-rise unreinforced masonry structures, Eng. Struct. 31 (2009) 125–137, https://doi.org/10.1016/j.engstruct.2008.07.021.

[54] B. Pulatsu, S. Gonen, E. Erdogmus, P.B. Lourenço, J.V. Lemos, J. Hazzard, Tensile fracture mechanism of masonry wallettes parallel to bed joints: a stochastic discontinuum analysis, Model Open Access J Model Eng Sci 1 (2020) 78–93, https://doi.org/10.3390/modelling1020006.

[55] S. Gonen, S. Soyoz, Reliability-based seismic performance of masonry arch bridges, Struct Infrastruct Eng (2021) 1–16, https://doi.org/10.1080/15732479.2021.1918726, 0.

[56] F. Parisi, N. Augenti, Uncertainty in seismic capacity of masonry buildings, Buildings 2 (2012) 218–230, https://doi.org/10.3390/buildings2030218.

[57] S. Saloustros, L. Pelà, F.R. Contrafatto, P. Roca, I. Petromichelakis, Analytical derivation of seismic fragility curves for historical masonry structures based on stochastic analysis of uncertain material parameters, Int. J. Architect. Herit. 13 (2019) 1142–1164, https://doi.org/10.1080/15583058.2019.1638992.

[58] N. Mojsilović, M.G. Stewart, Probability and structural reliability assessment of mortar joint thickness in load-bearing masonry walls, Struct. Saf. 52 (2015) 209–218, https://doi.org/10.1016/j.strusafe.2014.02.005.

[59] S. Gonen, B. Pulatsu, E. Erdogmus, P.B. Lourenço, S. Soyoz, Effects of spatial variability and correlation in stochastic discontinuum analysis of unreinforced masonry walls, Constr Build Mater 337 (2022) 127511, https://doi.org/10.1016/j.conbuildmat.2022.127511.

[60] S. Gonen, Reliability-based Seismic Assessment of Masonry Arch Bridges, Boğaziçi University, 2020.

[61] J. Pina-Henriques, P.B. Lourenço, Masonry compression: a numerical investigation at the meso-level, Eng. Comput. 23 (2006) 382–407, https://doi.org/10.1108/02644400610661163.

[62] J. Li, M.G. Stewart, M.J. Masia, S.J. Lawrence, Spatial correlation of material properties and structural strength of masonry in horizontal bending, J. Struct. Eng. 142 (2016), 04016112, https://doi.org/10.1061/(asce)st.1943-541x.0001488.

[63] M. Stein, Large sample properties of simulations using Latin hypercube sampling, Technometrics 29 (1987) 143–151, https://doi.org/10.1080/00401706.1987.10488205.

[64] B. Pulatsu, E. Erdogmus, E.M. Bretas, P.B. Lourenço, In-Plane Static Response of Dry-Joint Masonry Arch-Pier Structures, American Society of Civil Engineers, Reston, VA, 2019, pp. 240–248, https://doi.org/10.1061/9780784482261.028. AEI 2019.

[65] N. Mordà, A. Mancini, Norme tecniche per le costruzioni (NTC 2018), D. Min. Infrastrutture e Trasporti (2018), 17 gennaio 2018.

[66] C. Turco, M.F. Funari, S. Spadea, M. Ciantia, P.B. Lourenço, A digital tool based on Genetic Algorithms and Limit Analysis for the seismic assessment of historic masonry buildings, Procedia Struct. Integr. 28 (2020) 1511–1519, https://doi.org/10.1016/j.prostr.2020.10.124.

[67] M.F. Funari, A. Mehrotra, P.B. Lourenço, A tool for the rapid seismic assessment of historic masonry structures based on limit analysis optimisation and rocking dynamics, Appl. Sci. 11 (2021) 1–22, https://doi.org/10.3390/app11030942.

[68] M.G.D. Geers, V.G. Kouznetsova, W.A.M. Brekelmans, Multi-scale computational homogenization: trends and challenges, J. Comput. Appl. Math. 234 (2010) 2175–2182, https://doi.org/10.1016/j.cam.2009.08.077.

[69] M.F. Funari, B. Pulatsu, S. Szabó, P.B. Lourenço, A solution for the frictional resistance in macro-block limit analysis of non-periodic masonry, Structures 43 (2022) 847–859, https://doi.org/10.1016/j.istruc.2022.06.072.

[70] C. Casapulla, L. Argiento, Non-linear kinematic analysis of masonry walls out-of-plane loaded. The comparative role of friction between interlocked walls, Proc. Compdyn (2017) 15–17, 2017 6th ECCOMAS Themat. Conf. Comput. Methods Struct. Dyn. Earthq. Eng. Rhodes Island, Greece.

[71] M.F. Funari, S. Spadea, P. Lonetti, F. Fabbrocino, R. Luciano, Visual programming for structural assessment of out-of-plane mechanisms in historic masonry structures, J. Build. Eng. 31 (2020), 101425, https://doi.org/10.1016/j.jobe.2020.101425.